Mesocosm experiments identifying hotspots of groundwater upwelling in a water column by fibre optic distributed temperature sensing

Marruedo Arricibita, Amaya Irene; Krause, Stefan; Gomez-Velez, Jesus; Hannah, David M.; Lewandowski, Jörg

[Link to publication on Research at Birmingham portal](#)

RESEARCH ARTICLE

Mesocosm experiments identifying hotspots of groundwater upwelling in a water column by fibre optic distributed temperature sensing

Amaya Irene Marruedo Arricibita[1,2] | Stefan Krause[3] | Jesus Gomez-Velez[4] | David M. Hannah[3] | Jörg Lewandowski[1,2]

[1] Department of Ecohydrology, Leibniz-Institute of Freshwater Ecology and Inland Fisheries, 12587 Berlin, Germany

[2] Department of Geography, Humboldt University of Berlin, 10099 Berlin, Germany

[3] School of Geography, Earth and Environmental Sciences, University of Birmingham, B15 2TT, Birmingham, UK

[4] Department of Earth and Environmental Science, New Mexico Institute of Mining & Technology, Socorro, NM 87801, USA

Correspondence
Amaya Irene, Marruedo Arricibita, Department of Ecohydrology, Leibniz-Institute of Freshwater Ecology and Inland Fisheries, 12587 Berlin, Germany.
Email: marruedo@igb-berlin.de

Funding information
European Union's Seventh Framework, Grant/Award Number: 60715

Abstract

Lacustrine groundwater discharge (LGD) can substantially impact ecosystem characteristics and functions. Fibre optic distributed temperature sensing (FO-DTS) has been successfully used to locate groundwater discharge into lakes and rivers at the sediment–water interface, but locating groundwater discharge would be easier if it could be detected from the more accessible water surface. So far, it is not clear if how and under which conditions the LGD signal propagates through the water column to the water surface–atmosphere interface, and what perturbations and signal losses occur along this pathway. In the present study, LGD was simulated in a mesocosm experiment. Under winter conditions, water with temperatures of 14 to 16 °C was discharged at the bottom of a 10 × 2.8-m mesocosm. Water within this mesocosm ranged from 4.0 to 7.4 °C. Four layers (20, 40, 60, and 80 cm above the sediment) of the 82 cm deep mesocosm were equipped with FO-DTS for tracing thermal patterns in the mesocosm. Aims are (a) to test whether the positive buoyancy of relatively warm groundwater imported by LGD into shallow water bodies allows detection of LGD at the lake's water surface–atmosphere interface by FO-DTS, (b) to analyse the propagation of the temperature signal from the sediment-water interface through the water column, and (c) to learn more about detectability of the signal under different discharge rates and weather conditions. The experiments supported the benchmarking of scale dependencies and robustness of FO-DTS applications for measuring upwelling into aquatic environments and revealed that weather conditions can have important impacts on the detection of upwelling at water surface–atmosphere interfaces at larger scales.

KEYWORDS

lake, FO-DTS, heat tracer, jet, interface, driver

1 | INTRODUCTION

Lacustrine groundwater discharge (LGD), that is, the discharge of groundwater (GW) into lakes, can substantially impact ecosystem characteristics and functions (Baker et al., 2014; Ridgway & Blanchfield, 1998; Warren, Sebestyen, Josephson, Lepak, & Kraft, 2005). Upwards directed GW flow is sometimes called upwelling, especially in the context of hyporheic zones, where commonly both upwelling and downwelling occur along river reaches. In the present manuscript, we use the term upwelling solely for upward transport processes in the water column; this definition is adopted from limnophysics. On the one hand, upwelling of warm water in cold lakes can be caused by natural processes such as GW flow across the lake bed into the cold lake water body during winter conditions (LGD; Lewandowski, Meinikmann, Ruhtz, Pöschke, & Kirillin, 2013) or thermal springs in volcanic lakes (Cardenas et al., 2012). On the other hand, it can be related to thermal pollution

caused by industries such as electric power plants, which use water and discharge heated water into lakes and streams (Hung, Eldridge, Taricska, & Li, 2005; Shuster, 1986). In both cases, quantitative interpretations of warm water upwelling patterns are hampered by the lack of understanding of how the signal propagates from the sediment–water interface through the water column to the water surface–atmosphere interface and which perturbations and signal losses occur along this pathway. The present study will focus on LGD as an example of upwelling of warm water in lacustrine ecosystems during winter conditions due to its substantial impact on the ecosystem characteristics and functioning. LGD creates favourable habitats by affecting water chemical composition and temperature, supporting for instance the spawning of fish (Brunke & Gonser, 1997; Hayashi & Rosenberry, 2002). As climate warms, aquatic environments with strong GW influence are expected to support habitat stability and provide refuge for thermally stressed-aquatic species (Brabrand, Koestler, & Borgstrøm, 2002; Curry & Noakes, 1995; Hayashi & Rosenberry, 2002). Furthermore, detection of LGD is essential with respect to identifying it as a potential vector for pollution in aquatic ecosystems when GW quality is degraded (Nakayama & Watanabe, 2008). Despite the reported relevance of LGD on ecosystems, very little has been written about discharge of warm GW to lakes. Nearly all of the literature discusses discharge of cold GW to warm lakes, primarily because most of the research has been conducted during warm-water periods. Relatively cold GW has a higher density than warm lake water and, thus, would not reach the water surface.

There are no detailed field observations of how warm water propagates through the water column and to the surface of the lake during winter conditions. We address this research gap by looking at trigger conditions that allow upwelling of LGD from the sediment–water interface to the water surface atmosphere interface. We consider the temperature difference required between GW and surface water (SW) as well as the influence of meteorological conditions and diurnal cycles. The different temperatures of GW and SW might allow the detection of potential discrete areas of GW discharge to SW (Hare, Briggs, Rosenberry, Boutt, & Lane, 2015). Under the prerequisite of similar ion composition (which impacts water density), warm GW is less dense and more buoyant than cold SW, which allows upwelling of GW to the water surface. Thus, heat convection is augmented by density driven buoyant forces where warm GW discharges to cold SW. This process occurs during winter and early spring when SW is substantially colder than discharging GW and when the mixing is at a minimum at the lake surface (Hare et al., 2015; Lewandowski et al., 2013).

The basic concept of fibre optic distributed temperature (FO-DTS) technology is to analyse the temperatures monitored along specific distance intervals of a fibre optic cable based on (a) the travelling time of light in the optic fibre and (b) the temperature-dependent backscattering of light in the fibre (Selker, van de Giesen, Westhoff, Luxemburg, & Parlange, 2006). In this way, temperature can be monitored through the fibre optic cable up to a distance of several km, with spatial resolutions ranging from 0.3 to 4 m and measurement precision of 0.05 to 0.1 °C when sampling over 30-s intervals (Hausner et al., 2011; Selker, Thévenaz, et al., 2006; van de Giesen et al., 2012). FO-DTS has been used to detect GW discharge at the sediment–water interface of lakes (Blume, Krause, Meinikmann, & Lewandowski, 2013; Liu, Liu, Wang, & Zheng, 2015; Sebok et al., 2013) and streams (Krause,

Blume, & Cassidy, 2012; Lowry, Walker, Hunt, & Anderson, 2007). Here, FO-DTS is placed in layers of a specific depth above the sediment–water interface, to provide high-resolution temperature data to quantify the incidence, frequency, persistence, and attenuation of warmer discharging GW that reaches the water surface.

The aim of this study is to show that during winter, the positive buoyancy of relatively warm LGD to cold SW will allow or enhance detection of GW at the water surface–atmosphere interface (the lake surface). To address this aim, a mesocosm was used as a model system. Different layers of FO-DTS cable were deployed at different water depths to measure the temperature distribution. In addition, the following questions are addressed:

1. Which lake-internal upwelling patterns from the sediment–water interface through the water column to the water surface–atmosphere interface are caused by (simulated) LGD?

2. What are the intensities of (simulated) LGD at which GW signals can be identified at the water surface with FO-DTS?

3. What is the impact of weather conditions on detection of LGD at the water surface–atmosphere interface?

This paper addresses the research questions by (a) qualitative analysis of FO-DTS data, (b) statistical analysis of the FO-DTS data in order to describe temperature hotspots and significant spatial patterns across the water column, and (c) quantification of the effect of different weather conditions, injection rates, and the diurnal cycle on the net heat fluxes across the water surface (G, W m^{-2}) as well as the energy change due to advective transport by the water inlet from the lake and the water outlet from the mesocosm (E$_{adv}$ in MJ) and the change of internal energy in the mesocosm (ΔE in MJ). Section 4 presents a conceptual model based on analyses and limitations of FO-DTS data. The conclusions of the paper will summarize briefly the findings on the different data analyses carried out, answering the three research questions.

2 | MATERIAL AND METHODS

2.1 | Experimental set up

The mesocosm is composed of two inlets and one outlet (see Figure 1). Through one inlet water from Lake Müggelsee with a mean temperature of 4.7 °C was discharged with a rate of 33 L min^{-1}. The inlet was open throughout the experiment in order to keep homogeneous and relatively constant water temperatures and water levels. The second inlet comprised a hosepipe that was deployed on the bottom of the mesocosm to provide the warm water (14–16 °C measured at halfway between tap and mesocosm) injection. The hosepipe was insulated with insulation foam in order to reduce cooling of the injected water along the flow path from the tap (located in a building close to the mesocosm, 65-m distance). A nozzle was connected to the end of the hose and covered with a bag (35 × 35 cm) filled with sediment in order to most realistically simulate discrete LGD at the sediment–water interface. Finally, an outlet on the opposite side to the cold water inlet assured a constant water level in the mesocosm of 0.82 m height. The outlet discharge rates varied from 34 to 48 L min^{-1} depending on the applied warm water injection rate.
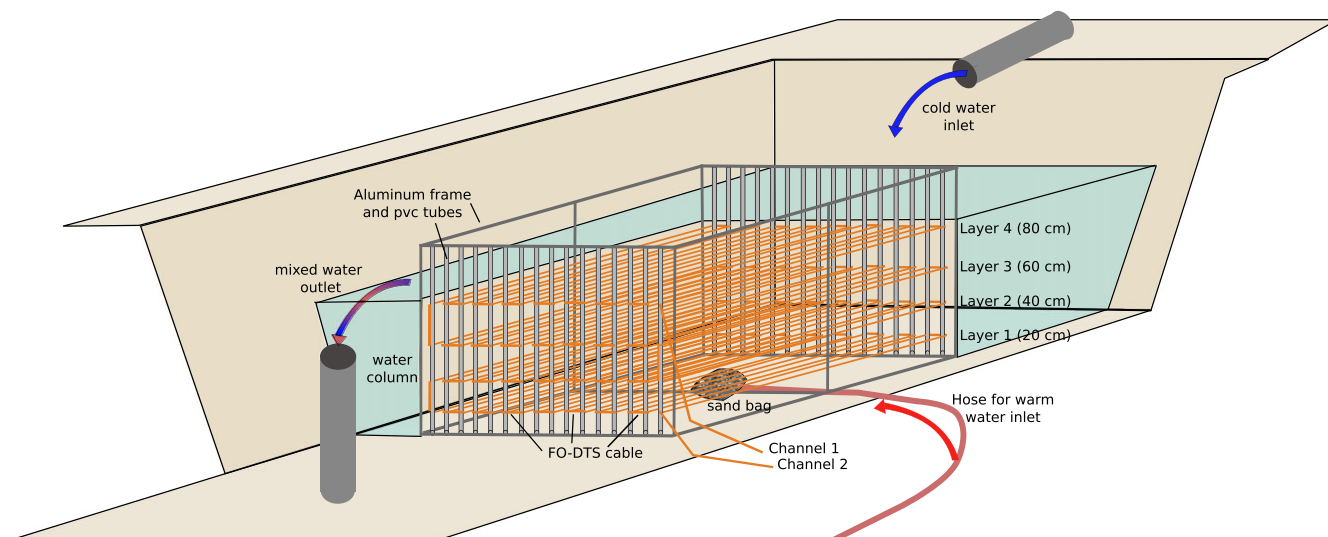
FIGURE 1 Sketch of the experimental set up showing a cross section through the mesocosm including the fibre optic distributed temperature sensing set up

An aluminium frame with dimensions: 4 m × 2 m and 1.5 m height was used to deploy the FO-DTS cable at different water depths (Figure 1). The FO cable was installed in four layers at different heights: 20, 40, 60, and 80 cm (Layers 1, 2, 3, and 4, respectively) above the bottom of the mesocosm (Figure 1). The FO-DTS cable was routed back and forth across the aluminium frame in a rectangular grid formation so that 15 parallel reaches of the cable extended across each layer within the mesocosm. Temperatures were averaged over 12.5-cm intervals (sampling resolution) along the FO-DTS cable. We acknowledge that the presence of the FO cable may alter the flow of water and heat within the mesocosm; however, considering the cable volume (0.009%) compared to the water volume and the spacing between cables (at least 12.5 cm), the effect is probably minor.

From March 11, 2015, to March 27, 2015, seven 24-hr temperature datasets were obtained: one control dataset without warm water injection under overcast conditions; three datasets with 1 L min^{-1} injection rate, under clear, partly cloudy, and overcast conditions, respectively; two datasets with 5 to 5.5 L min^{-1} injection rate, under clear and overcast conditions, respectively; and finally, one dataset with 15 L min^{-1} injection rate under overcast conditions.

Measurements were carried out using an ULTIMA-S DTS (SILIXA Ltd.) with a sampling resolution of 12.5 cm and spatial resolution of approximately 30 cm. DTS sampling resolution depends on the duration of each of the laser pulses sent by the DTS. For example, a DTS sending laser pulses of 10 ns has a sampling resolution of 1 m, the ULTIMA-S, with a sampling resolution of 12.5 cm, sends pulses of 1.25 ns. The spatial resolution refers to the distance between points along the FO cable located next to an abrupt change on temperature in a way that the point on the low side is not placed higher than 10% of the abrupt jump and the point on the high side is placed higher than 90% of the abrupt jump (Selker, Tyler, & Van de Giesen, 2014).

Five hundred metres of multimode FO cable from Silixa Ltd., were deployed for the experiments of this study. Using a multimode fibre allowed flexible bending and thus supported an adequate set up of the cable in the aluminium frame.

2.1.1 | Simulated upwelling flux rates versus rates reported in literature

The LGD rates used in the present study are based on measured flow rates in the tube (1 to 15 L min^{-1}) used for injecting warm water into the mesocosm. The tube outlet is covered by a sand bag to simulate discrete LGD from sediments. An uncovered tube outlet might have caused a jet stream that would be quite unrealistic for LGD and therefore was avoided. The LGD rate can be referred to different areas: (a) the sand bag covering the tube outlet (35 × 35 cm) resulting in 8.2 to 122.4 L m^{-2} min^{-1}, (b) a square metre, that is, 1 to 15 L m^{-2} min^{-1}, and (c) the entire mesocosm (10 × 2.8 × 0.82 m) resulting in 0.036 to 0.536 L m^{-2} min^{-1}. The latter approach is often used in lake studies in which the total exfiltration is related to the entire lakebed.

The LGD rates applied in the present mesocosm experiment are at the upper end of LGD rates occurring in situ. Rosenberry, Lewandowski, Meinikmann, and Nützmann (2015) reviewed the international literature and report a median exfiltration rate of 0.74 cm day^{-1} (=0.005 L m^{-2} min^{-1}) and a maximum of 745 cm day^{-1} (=5.2 L m^{-2} min^{-1}). The maximum of 745 cm day^{-1} is a point estimate based on seepage metre measurements (Kidmose, Engesgaard, Nilsson, Laier, & Looms, 2011). A high rate referred to the entire lake bed is reported by Piña-Ochoa and Lvarez-Cobelas (2009), which is 0.05 to 0.1 L m^{-2} day^{-1}. For punctual focused LGD much higher rates are possible: For example, in Norrström and Jacks (1996) macropore GW discharge rates of 18 and 42 L min^{-1} are reported for areas of 0.0078 and 0.031 m^2. More extreme examples can be found in natural thermal ponds or pools with hot springs with up to 800 L min^{-1} discharge rates (Haselwimmer, Prakash, & Holdmann, 2013). Intense warm water discharge might also be of anthropogenic origin such as sewage leakage from under water pipes (Apperl, Pressl, & Schulz, 2017).

2.1.2 | Measurement protocol and calibration

Once the FO cable was properly deployed onto the aluminium frame, the exact start and end positions of each cable line were identified.

This was done by locally warming the cable at each bend, identifying the temperature peak on the data output graph, and noting the distance along the cable at this peak. This allowed locating of each of the four fibre optic layers, including their start and end points, as well as the beginning and end of each FO cable sequence.

Calibration of the FO-DTS by temperature offset correction was carried out using an external probe of the DTS device and FO cable reference sections within an isolated ice bath with a mix of ice and water that assured constantly 0 °C. For the differential loss correction, the fixed value setting was chosen along the relatively short cable (500 m) without any splices. A default value of 0.255 dB/km was used as this value is the expected value for Corning ClearCurve™ OM3 fibre.

An alternate single-ended measurement set up was used with alternating monitoring direction of the light pulse sent from the DTS device. Measurements were averaged at 10-s intervals (integration time) in each direction. This means that the time interval between measurements from the same channel was 20 s.

2.2 | Data analyses and spatial statistics

All data analysis, including summarizing statistics for quantification of spatial patterns and statistical relationships of observed data within layers and between layers, was conducted in R and ArcGIS. The following spatial statistical metrics were quantified:

2.2.1 | Moran's *I* and Moran scatter plot of testing spatial autocorrelation

The Moran's *I* values were calculated as indicators of the degree of linear association between a value in a specific location (*x*-axis) and surrounding locations (*y*-axis). Moran's *I* scatter plots were used to visualize the type and strength of spatial autocorrelation of observed temperatures. The four quadrants of the Moran's *I* scatter plot indicate, from *x*-axis to *y*-axis: high-high and low-low quadrants contain values with positive spatial autocorrelation and high-low and low-high quadrants contain values with negative spatial autocorrelations. The Moran's *I* scatter plot displays a "spatially lagged" transformation of a variable (in *y*-axis) on the original spatial variable (in *x*-axis). In addition, the Moran's *I* scatter plot reports the summary of potential influential

observations (highlighted in red diamond shape in Moran's *I* scatter plot) for the linear relationship between the data and the lag. Finally, the slope of the scatter plot indicates Moran's *I* values obtained and the overall spatial autocorrelation of the dataset (Anselin, 1996; Bivand, Pebesma, & Gómez-Rubio, 2013).

2.2.2 | Local indicators of spatial association maps

Local indicators of spatial association (LISA) have been calculated to identify significant spatial clusters or outliers that have been used in this study to highlight local hotspots of simulated warm water upwelling. The clusters and spatial outliers of LISA maps correspond to the four quadrants of the Moran's *I* scatter plots, providing a measure of clusters or outliers that are of statistical significance (Anselin, 1995).

2.2.3 | Spatial correlation between layers: Band collection statistics

Band collection statistics conducted in AcrGIS allowed the analysis of sets of raster bands, in the present study a set of 4 FO-DTS temperature layers. Covariance and correlation matrices and basic statistical parameters (minimum, maximum, mean, and standard deviation) for each layer have been calculated. The covariance matrix indicates for each layer how much variance is from the mean value of each layer. The correlation matrix shows how correlated the cell values of one layer are to the cell values of another layer (Environmental Systems Research Institute, 2014).

2.3 | Preprocessing and sources of error

Figure 2a shows temperature data of a single measurement point on the FO cable over 24 hr of measurement (black line) with a clear diurnal trend. However, noise is predominant on the plotted curve. Noise can be related to the sensor, turbulence, and short time fluctuations of weather conditions (sunlight/no sunlight). In order to clear the temperature signal, local polynomial regression fitting (LOESS) was applied in R. The red line in Figure 2a represents the fitted curve. Applying LOESS to the raw temperature resulted in removal of noise from the data ranging from 0.0 to 0.6 °C (Figure 2b).
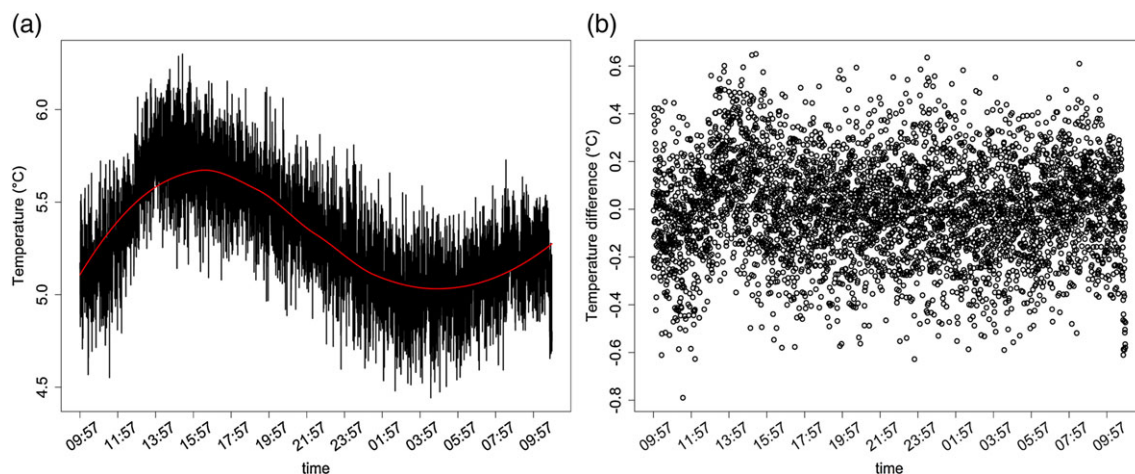

FIGURE 2 (a) Raw temperature data (black line) and smoothed temperature data with local polynomial regression fitting (LOESS; red line) and (b) temperature difference between raw temperature data and smoothed temperature data

2.4 | Quantification of net heat fluxes across the water surface, advective heat fluxes, and internal energy change

In order to identify the main drivers affecting the spatial patterns observed within the water column (Figure 3), heat losses and gains at the mesocosm surface have been quantified. Steady state water flow of the mesocosm has been assumed. G, ΔE, and net-advective heat flux (E_{adv} in MJ) have been calculated following equations in Appendix S1. E_{adv} consists of cold and warm water inputs to the mesocosm and the water flow out of the mesocosm.

3 | RESULTS

3.1 | FO-DTS observed temperature patterns

Spatial linear interpolations of time averaged values (day and night separately) from 24-hr measurements are shown in Figure 3. The slice3D plots integrate the four layers of FO-DTS temperature measurements. The plots show the temperature differences from the minimum temperatures (ΔT_{min} in degrees [°C]) of each dataset with the same colour scale for both day and night. Because the present figure is focusing on spatial patterns of warm water upwelling, and not

on quantifying upwelling per se, we did not use absolute temperature values. In addition, ΔT_{min} values show the intensity of the warm water hotspots in the water column and in the water surface for all three injection rates in each dataset.

The plots allow tracing of the warm water injected at the bottom of the mesocosm with rates of 1, 5–5.5, or 15 L min⁻¹, respectively, and its propagation through the water column. These plots represent averaged values of measurements taken during day and night separately. Figure 3a–c represents the ΔT_{min} observed in experiments under clear or partly cloudy conditions. Although the source of warm water can clearly be detected at the bottom of the mesocosm, its impact on observed ΔT_{min} spatial patterns is vanishing with increasing distance from the source in the upper layers.

In contrast, Figure 3d–f represents ΔT_{min} observed in each experiment under overcast conditions. Injected warm water can be traced in all four layers at all applied injection rates: 1, 5, and 15 L min⁻¹. In addition, night measurements show clearer spatial patterns than day measurements. Finally, depending on the applied injection rate, the upwelling of warm water from the bottom shows different flow paths (see Figure 3d–f). The different flow paths observed in Figure 3d–f are related to the cold water inlet on the right side of the mesocosm. The cold water inlet created a vortex from the right side of the mesocosm to left, and the injected warm water moved
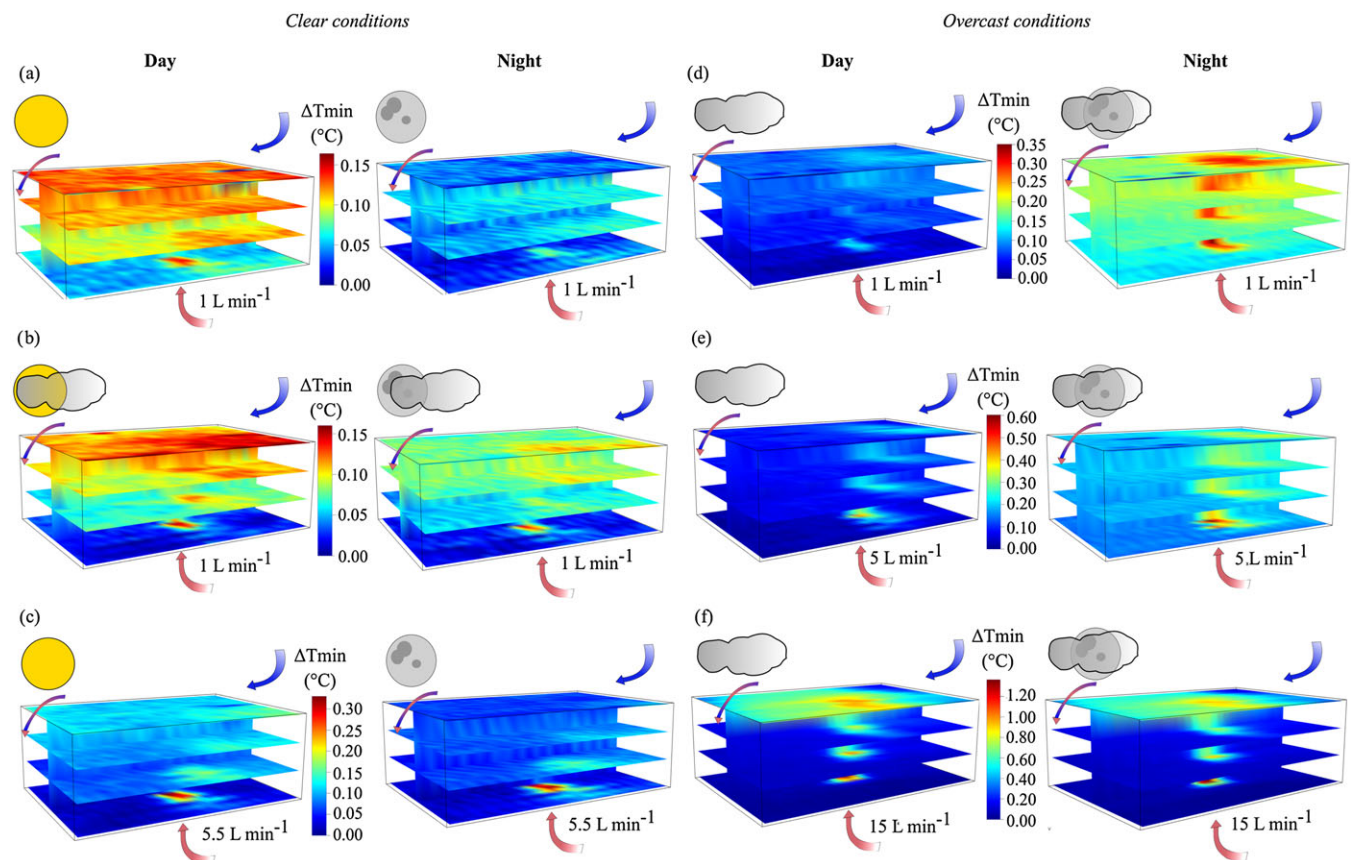
FIGURE 3 Slice3D plots visualizing for the four layers of DTS measurements the difference from the minimum temperature of each dataset. Values averaged for approximately 12 hr day (always left of colour scale) or night (always right), respectively. Different injection rates and weather conditions as follows: (a) 1 L min⁻¹ clear 19.03.2015, (b) 1 L min⁻¹ partly cloudy 25.03.2015, (c) 5.5 L min⁻¹ clear 18.03.2015, (d) 1 L min⁻¹ overcast 26.03.2015, (e) 5 L min⁻¹ overcast 27.03.2015, and (f) 15 L min⁻¹ overcast 12.03.2015. ⤷ inlet of cold lake water, ⤷ inlet of warm water, ⤷ outlet of mixed water from mesocosm. ● clear day, ● clear night, ☁ partly cloudy day, ☁ partly cloudy night, ☁ overcast day, and ☁ overcast night

along with this vortex. In Figure 3f, this effect is also visible on the top layer. Due to the high injection rate (15 L min^{-1}), the warm water flows straight up to the SW in Figure 3f.

3.2 | Quantitative analysis of spatial temperature patterns

3.2.1 | Horizontal spatial temperature patterns: Spatial autocorrelation within layers: Moran's *I* scatter plots and LISA maps

All datasets show significant spatial autocorrelation between data points within each layer with *p* values less than 2.2 e^{-16}, except the dataset of Layer 3 at an injection rate of 1 L min^{-1} at night under clear sky conditions where the *p* value is 1.18 e^{-06}. As an example, Figure 4 compares the Moran's *I* scatter plots and LISA maps during daytime for 1 L min^{-1} clear sky and 15 L min^{-1} overcast sky conditions. When injecting 1 L min^{-1} with clear sky conditions, despite the significant spatial autocorrelation, the temperature data values are more dispersed over the four quadrants. Figure 4a indicates potential influential observations in Layers 1 and 2, mainly located in the quadrant "high-high," identifying a positive spatial autocorrelation between observation points surrounding those data values. However, in Layers 3 and 4 (Figure 4a), the distribution of potential influential observations over the four quadrants is more dispersed, not showing

a clear clustering of points on "high-high" and "low-low" quadrants (in red and yellow in LISA maps, Figure 4c).

On the contrary, temperatures observed for the 15 L min^{-1} injection rate show stronger spatial autocorrelation with most of the data points in high-high and low-low quadrants indicating a positive spatial autocorrelation (Figure 4b and 4d). Thus, the spatial autocorrelation over the four layers is stronger than in the dataset of 1 L min^{-1} and clear sky condition. Furthermore, LISA maps (Figure 4 d) show a clear clustering of the highly spatially autocorrelated values.

Calculated Moran's *I* values in Figure 5 compare the intensity of spatial autocorrelation between the temperature data points for different weather conditions and day or night observations within each layer. In all cases, Moran's *I* values increase from the lowest to the highest injection rates (Figure 5). The injection of warm water has a larger impact on the temperature patterns observed in the upper layers at higher injection rates. In general, all layers show highest Moran's *I* values when the measurements were obtained under overcast weather conditions. Layers 3 and 4 (uppermost layers in the water column) show the highest increase in Moran's *I* values under overcast weather conditions at injection rates of 1 and 5 L min^{-1} injection rates.

Moran's *I* values for Layers 1 and 2 (closest to the warm water injection) were high under all weather conditions. This indicates a higher influence of warm water inflow on temperature patterns observed in Layers 1 and 2 than in Layers 3 and 4.
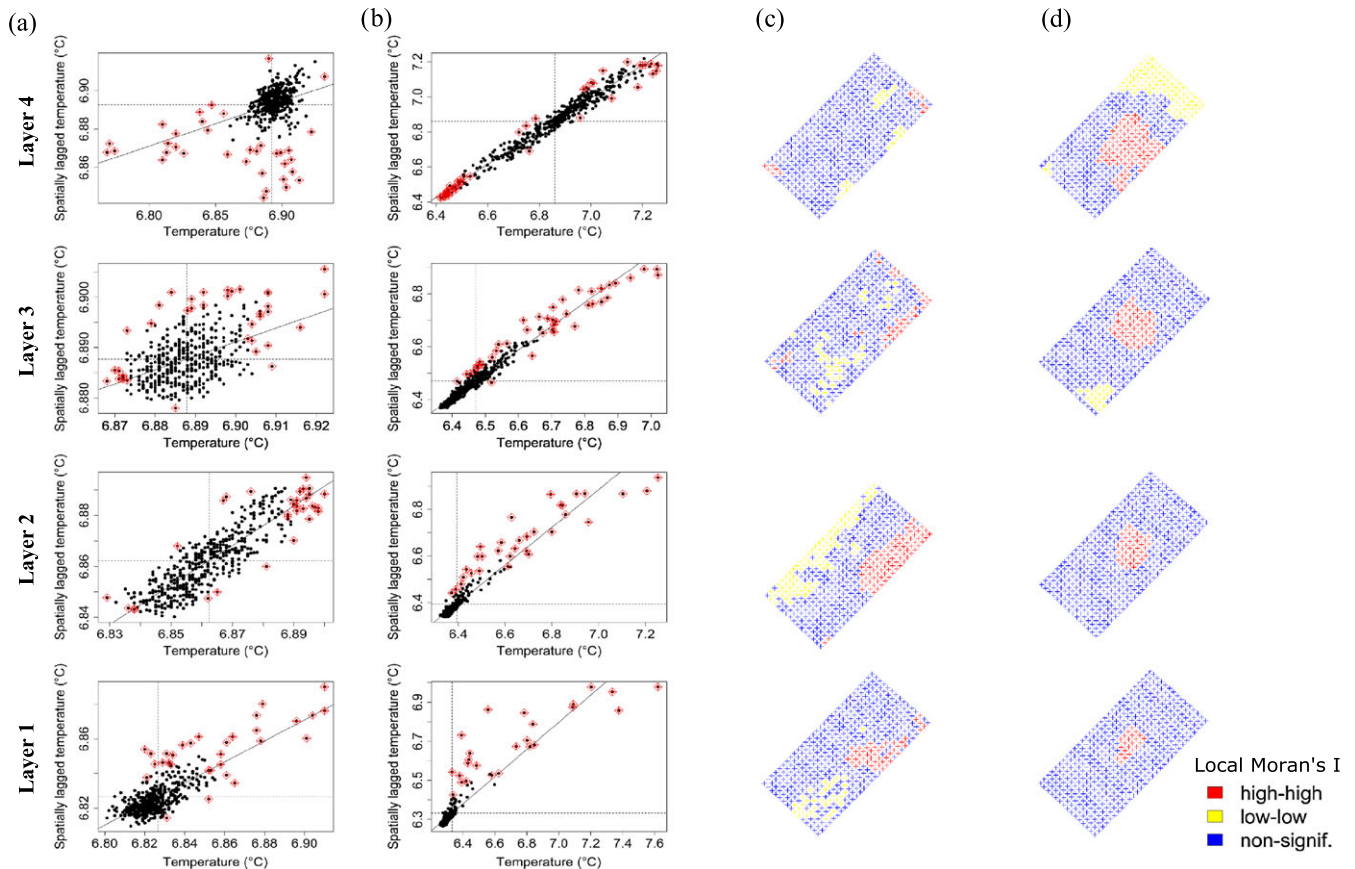
FIGURE 4 (a) and (b) Moran's *I* scatterplots, (c) and (d) LISA maps, (a) and (c) for 1 L min^{-1} clear sky, day, (b) and (d) for 15 L min^{-1} overcast sky, day. In (a) and (b), potential influencing measures for the linear relationship between the data and the lag are highlighted as red diamond shape. In (c) and (d), red coloured points belong to the high-high quadrant in Moran's *I* scatterplot, yellow coloured points belong to the low-low quadrant in Moran's *I* scatterplot, and blue coloured points are spatially nonsignificant points. From top row to bottom row: Layers 4, 3, 2, and 1
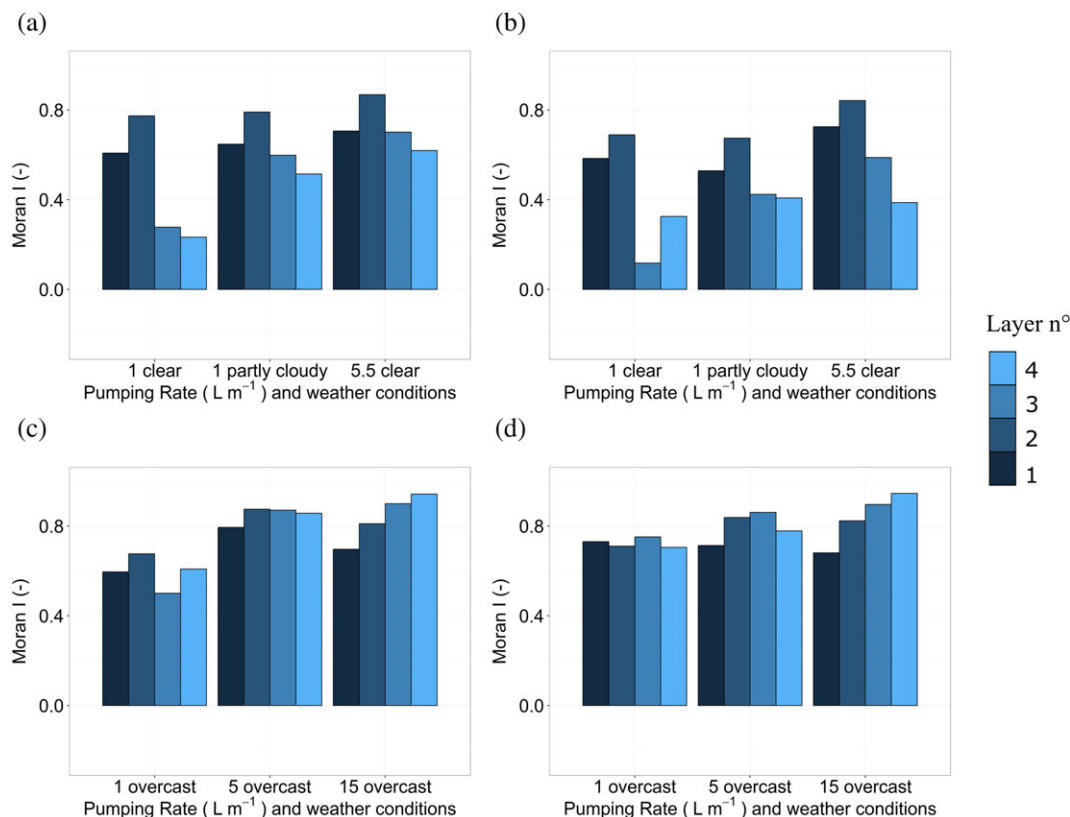
FIGURE 5 Moran's *I* values. (a) Day, clear and partly cloudy sky; (b) night, clear and partly cloudy sky; (c) day, overcast sky; and (d) night, overcast sky. All plots are plotted from lowest to highest injection rates

Under clear sky weather conditions, Moran's *I* values for Layers 1 and 2 are similar or decrease slightly during night measurements. For Layers 3 and 4, Moran's *I* values during night are lower than Moran's *I* values during day measurements.

Under overcast weather conditions, Moran's *I* values within Layers 1, 2, 3, and 4 for 1 L min^{-1} injection rate increase during night measurements. For an injection rate of 5 L min^{-1}, Moran's *I* values for Layers 1 and 4 are lower during night than during day measurements. Finally, Moran's *I* values for 15 L min^{-1} injection rate are very similar during day and night measurements.

In summary, significant spatial autocorrelations within each layer have been identified in all datasets. However, calculated Moran's *I* values vary depending on the injection rate of warm water, weather conditions, and the diurnal cycle (see Figure 5). This indicates that the strength of the spatial pattern within each layer also varies depending on the injection rates applied, the weather conditions, and the diurnal cycle.

3.2.2 | Vertical spatial temperature patterns: Spatial correlation between layers

Spatial correlation between neighbouring layers
At high injection rates, the largest correlations between neighbouring layers occurred (Table S1). At lower injection rates, the correlation was usually much smaller and the largest correlation generally occurred between neighbouring layers. There are three exceptions where the largest correlations occurred between nonneighbouring layers: dataset 1 L min^{-1}, clear, daytime and 1 L min^{-1}, partly cloudy, day and night-time. The reason might be that the extent of the spatial warm water pattern in

Layers 1 and 3 is more similar than the observed pattern in Layer 2 (See Figures 4c and **S1**).

Measurements under clear sky conditions with an injection rate of 1 L min^{-1} showed a downward trend (from Layer 1 to 4) on spatial correlation coefficients calculated between neighbouring layers (1&2, 2&3, 3&4). When weather conditions were "partly cloudy" for 1 L min^{-1}, spatial correlation coefficients calculated between neighbouring layers showed an upward trend from Layer 1 to 3 (1&2 and 2&3) and the lowest value between the two uppermost layers (3&4). Finally, when weather conditions were overcast and injecting 1 L min^{-1}, it is possible to see that there was an upward trend (from Layer 1 to 4) on spatial correlation coefficients calculated between neighbouring layers (1&2, 2&3, 3&4), for example, from 0.415 to 0.815 during day.

The same upward trend was observed for an injection rate of 5.5 L min^{-1} with clear sky conditions for spatial correlation coefficients calculated between neighbouring layers: from 0.516 to 0.685. At injection rate of 5 L min^{-1} with overcast conditions, spatial correlation coefficients between neighbouring layers keep increasing, for example, from 0.795 to 0.933 day.

On the contrary, when injecting 15 L min^{-1}, calculated spatial correlation coefficients between neighbouring layers only increase for layers 1&2 and 2&3 from 0.846 to 0.888. Spatial correlation coefficients for 3&4 layers decrease to 0.450.

Spatial correlation between nonneighbouring layers
Highest spatial correlations calculated between nonneighbouring layers (1&3, 1&4, and 2&4) were found for 1 L min^{-1} under overcast conditions during night (0.681, 0.572, and 0.663, respectively) and

for 5 L min^{-1} under overcast conditions during day (0.608, 0.546, and 0.791, respectively).

Spatial correlation coefficients between Layers 1&3 generally increase from 1 to 15 L min^{-1} under overcast conditions. Spatial correlation coefficients between layers 1&4 and 2&4 generally increase from 1 to 5 L min^{-1} and considerably decrease at 15 L min^{-1}. These observations agree with the change on the spatial pattern observed in Figure 3f, compared with the spatial patterns observed in Figures 3d and 3e. In Figure 3f, injected warm water flows straight up across Layers 1, 2, and 3. In Layer 4, injected warm water spreads all over the water surface. Low spatial correlation coefficients for 15 L min^{-1} between Layers 2&4 and 1&4 indicate differences of spatial patterns observed between Layers 1&4 and 2&4 in Figure 3f.

Figure 6 presents calculated spatial correlation coefficients for different (clear sky, partly cloudy, and overcast) conditions for both day and night measurements independently.

Spatial correlation coefficients calculated between 1&2, 1&3, and 2&3 are higher during night than during day. However, spatial correlation coefficients calculated for 1&4, 2&4, and 3&4 showed different results. For clear sky conditions, calculated spatial correlation coefficients during night time are lower than calculated spatial correlation coefficients for the same injection rates during day. In contrast, calculated spatial correlation coefficients for overcast weather conditions are slightly higher during night than during day within the same injection rates, for both 1 and 15 L min^{-1}. In contrast, for 5 L min^{-1} under overcast conditions, spatial correlation coefficients are slightly lower during night than during day.

Three main findings can be listed from the calculation of spatial correlation coefficients between layers:

- In general, overcast weather conditions result in higher spatial correlation coefficients between neighbouring layers and nonneighbouring layers.

- At 15 L min^{-1}, the uppermost layer (Layer 4) is spatially less correlated with the underlying layers than at 1 and 5 L min^{-1} under overcast conditions. These observations agree with the change on the spatial pattern observed in Figure 3f in comparison with the spatial patterns observed in Figure 3d,e.

- The diurnal cycle has an effect on spatial correlation coefficients calculated between layers. Layers within the water column show higher spatial correlation coefficients between them during night than during day for the same injection rates no matter of the weather conditions. However, for the uppermost layer (Layer 4) at the water surface–atmosphere interface, spatial correlation coefficients are lower for clear nights and generally similar or slightly higher for overcast nights.

3.3 | Net heat fluxes across the water surface, advective heat fluxes, and internal energy change

The effects of different weather conditions, different injection rates, and the diurnal cycle on the energy balance of the water column were quantified. This was done by quantifying the net heat fluxes across the
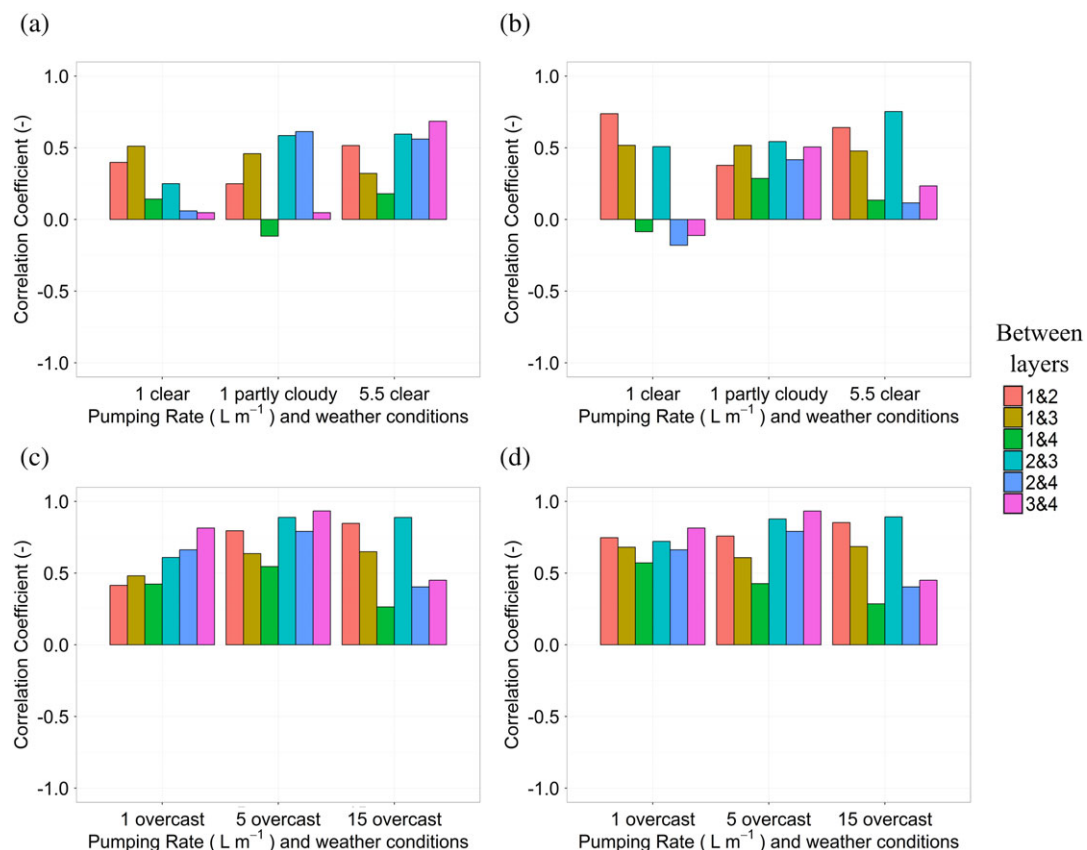

FIGURE 6 Spatial correlation coefficients for (a) day, clear sky and partly cloudy conditions; (b) night and clear sky, partly cloudy conditions; (c) day and overcast conditions; (d) night and overcast conditions

water surface (G in W m^{-2}) as well as the energy change due to advective transport by the water inlet from the lake, the warm water inlet at the bottom of the mesocosm and the water outlet from the mesocosm (E_{adv} in MJ). Their sum results in the change of internal energy in the mesocosm (ΔE in MJ).

Net heat fluxes across the water surface (G)

Net heat fluxes across the water surface (G) during day and night are composed of net radiation (R_n), latent heat fluxes (phase transformation, λE), and sensible heat fluxes (H) with R_n being the most important of the three (see Figure 7a,c,e,g,i,k,m). This indicates that the system gains and loses energy mainly by R_n.

Net radiation (R_n) is composed of net shortwave radiation (R_{ns}) and net longwave radiation (R_{nl}). The net shortwave radiation (R_{ns}) is considered a heating term (during daytime) and the net longwave radiation (R_{nl}) is considered a cooling term (during day and night; Betts, 2015). Therefore, during daytime, calculated R_n values are higher than during night for both clear and overcast weather conditions (Figure 7a,

c,e,g,i,k,m). This is because during daytime, the surface cooling due to R_{nl} is partly compensated by R_{ns} (Betts, 2003, 2015; Betts, Desjardins, & Worth, 2013). In addition, during night, there is no shortwave radiation coming from the sun and the cooling term, R_{nl}, will be the main component of the R_n.

In general, R_n values during daytime are lower under overcast weather conditions than under clear sky conditions (Figure 7a,c,e,g,i, k,m). During night, R_n values are less negative under overcast conditions than under clear sky conditions (Figure 7a,c,e,g,i,k,m). These results are related to the important effect that clouds have on the net radiation balance (R_n; Betts, 2015). On the one hand, during daytime, incident downward shortwave radiation at the water surface is lower under overcast weather conditions than under clear sky conditions. On the other hand, during day and night, surface cooling to space due to R_{nl} is lower under overcast weather conditions than under clear sky conditions (Betts, 2003, 2015; Betts et al., 2013). The smallest net heat fluxes across the water surface (G) occur under overcast conditions (see Figure 7a,g,k,m).
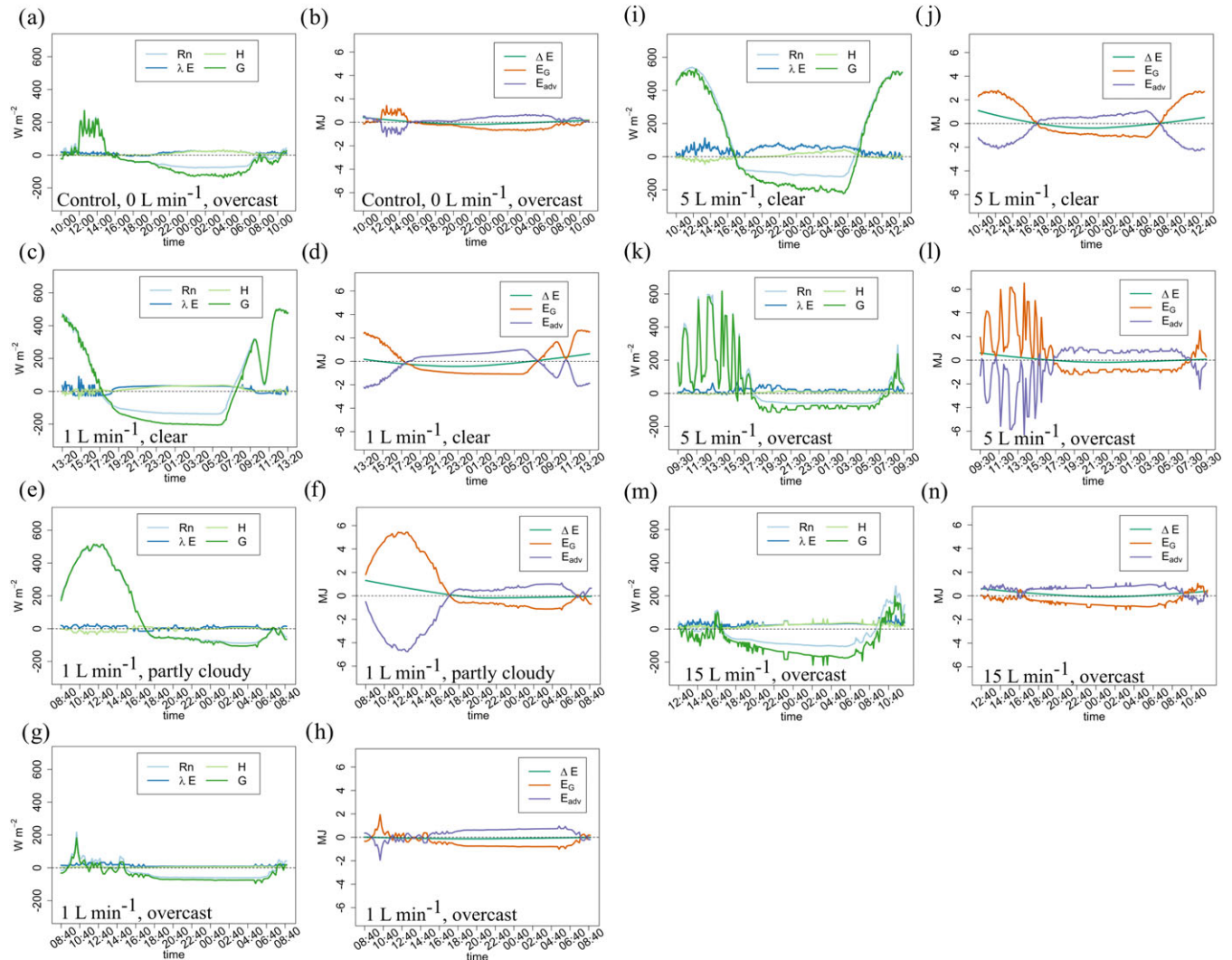
FIGURE 7 Calculated heat fluxes across the water surface (G), net radiation (Rn) evaporative heat flux (λE), and sensible heat flux (H) for (a) control dataset with 0 L min^{-1} injection rate, overcast, (c) 1 L min^{-1} clear, (e) 1 L min^{-1} partly cloudy, (g) 1 L min^{-1} overcast, (i) 5.5 L min^{-1} clear, (k) 5 L min^{-1} overcast, and (m) 15 L min^{-1} overcast and calculated ΔE, EG and E_{adv} for (b) control experiment overcast (d) 1 L min^{-1} clear (f) 1 L min^{-1} partly cloudy, (h) 1 L min^{-1} overcast, (j) 5.5 L min^{-1} clear, (l) 5 L min^{-1} overcast, and (n) 15 L min^{-1} overcast

Energy transferred across the interface (E$_G$) and advected energy by inflows and outflows (E$_{adv}$)

For all datasets, during daytime measurements, the system gains energy mainly by E$_G$ and during night time measurements by E$_{adv}$ (Figure 7b,d,f, h,j,l). Only, for 15 L min^{-1} overcast weather conditions dataset, the system mainly gains energy by E$_{adv}$ during day and night due to the high amounts of injected warm water (Figure 7n). This means that the energy gains in the mesocosm during day are dominated by the net heat fluxes across the water surface (G) and the energy losses in the mesocosm are dominated by the energy transported by advection into and out of the mesocosm. On the contrary, the energy gains in the mesososm during night are dominated by the imported energy of the injected warm water (E$_{adv}$) and the energy losses in the mesocosm are dominated by the net heat fluxes across the water surface (G).

Internal energy changes in the mesocosm (ΔE)

ΔE changes over time are clearly affected by the diurnal cycle (see Figure 8). ΔE decreases during the day; it reaches a minimum during night and increases again in the early morning. However, the intensity of changes of ΔE over time varies depending on weather conditions and injection rate.

ΔE changes over time are lowest under overcast weather conditions for all different injection rates. The dataset with an injection rate of 1 L min^{-1} shows the lowest ΔE changes over time, and 15 L min^{-1} shows the highest ΔE changes over time.

High changes on ΔE over time are observed when injecting 1 L min^{-1} under clear sky conditions. For partly cloudy conditions, keeping the same injection rate, the maximum loss of energy over time is smaller than under clear sky weather conditions. However, the slope of ΔE in Figure 8 for 1 L min^{-1} partly cloudy is higher than that of the 1 L min^{-1} clear sky during day; this indicates that the rate of energy loss is greater. On increasing the injection rate to 5.5 L min^{-1} under clear sky, maximum energy loss in the system is almost similar to the maximum energy loss when injecting 1 L min^{-1} under clear sky. However, change of ΔE over time is greater when injecting 5.5 L min^{-1} under clear sky than when injecting 1 L min^{-1} under clear sky.
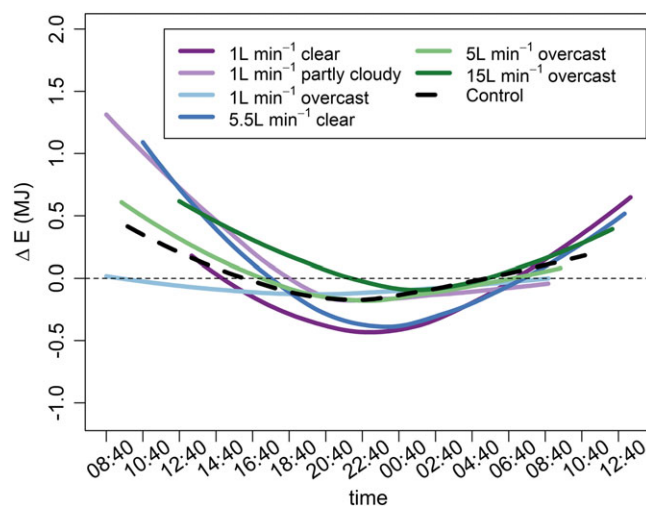
FIGURE 8 Change of energy (ΔE) over time for seven datasets: 1 L min^{-1} clear, 1 L min^{-1} partly cloudy, 1 L min^{-1} overcast, 5.5 L min^{-1} clear, 5 L min^{-1} overcast, 15 L min^{-1} overcast, and control dataset with 0 L min^{-1} injection rate, overcast conditions

Coupling internal energy changes over time (ΔE), net heat fluxes across the water surface (G) and energy in the mesocosm (E$_G$ and E$_{adv}$)

Under overcast conditions, energy changes (ΔE) in the mesocosm are lower and slower than energy changes (ΔE) in the mesocosm under clear sky conditions. This can be related to the calculated small net heat fluxes across the water surface (G) under overcast conditions. Or in other words, energy at the water surface is lost at smaller quantities and at slower rates under overcast conditions than under clear sky. As the amount of injected warm water increases, the amount of advected energy (E$_{adv}$) in the mesocosm increases. Under clear sky, net heat fluxes across the water surface (G) are bigger than under overcast weather conditions. Higher injection rates of warm water under clear sky will result in higher and faster energy changes (ΔE) over time in the mesocosm due to bigger net heat fluxes across the water surface (G). On the contrary, under overcast conditions, higher injection rates of warm water will contribute to decrease and to slow down the energy changes (ΔE) over time in the mesocosm, due to small net heat fluxes across the water surface (G).

Finally, during daytime, because R$_n$ is the main component of the net heat fluxes across the water surface (G), the mesocosm energy gains are due to R$_n$ (R$_{ns}$ and R$_{nl}$). This agrees with E$_G$ being the main driver of gains of energy in the mesocosm during daytime. If the mesocosm is subject to strong gains of energy due to R$_n$ during day (for instance under clear sky), it means that energy gains by R$_{ns}$ will prevail over energy losses by R$_{nl}$. During night, the main losses of energy in the mesocosm are driven by R$_n$ (only R$_{nl}$). This agrees with E$_G$ being the main driver of losses of energy in the mesocosm during night.

Observed spatial patterns of injected warm water in the mesocosm, net heat fluxes across the water surface (G), and energy changes over time (ΔE)

Spatial patterns of injected warm water across the water column and at the water surface observed in Figure 3d–f can be related to small and slow energy changes (ΔE) over time, due to small net heat fluxes across the water surface (G) under overcast weather conditions during day and night. During daytime, the heat signal of the injected warm water will prevail across the water column and at the water surface due to: 1) less absorbed shortwave radiation at the water surface of the mesocosm (R$_{ns}$) and 2) less water surface cooling in the mesocosm due to R$_{nl}$. During night-time, the heat signal of the injected warm water will prevail across the water column and at the water surface due to: 1) less water surface cooling in the mesocosm due to R$_{nl}$ and 2) energy gains in the mesocosm due to injected warm water.

Finally, spatial patterns of injected warm water, across the water column and at the water surface, observed in Figure 3a–c can be related to high and fast energy changes (ΔE) over time in the mesocosm, due to stronger net heat fluxes across the water surface (G) under clear sky during day and night, than under overcast conditions. In general, during daytime, the heat signal of the injected warm water is not detectable at the water surface, mainly due to high amount of absorbed shortwave radiation at the water surface (R$_{ns}$) during clear sky and to a less extent, due to water surface cooling in the mesocosm by R$_{nl}$. During night, the heat signal of the injected

warm water is not detectable at the water surface due to strong cooling of the water surface in the mesocosm by R_{nl}.

4 | DISCUSSION

4.1 | Detectability of upwelling signals

One basic question of the present study is if and under which circumstances the lake-internal upwelling pattern due to simulated GW discharge can be detected in the water column and at the water surface. For that purpose, temperature signals due to the positive buoyancy of relatively warm water need to be separated from other temperature fluctuations. In the context of the present study, strong spatial autocorrelations within layers and strong spatial correlations between layers are interpreted as "real" temperature signal related to the positive buoyancy of relatively warm water, instead of to other temperature fluctuations. Moran's I and LISA maps (indicators for horizontal spatial patterns within layers) confirmed the spatial patterns visually observed in Figure 3. The strength of spatial autocorrelation within layers (horizontal spatial patterns) increased under overcast conditions, at higher injection rates and during night-time. Calculated spatial correlation coefficients between layers (vertical spatial patterns) also increased under overcast weather conditions, higher injection rates, and during night-time measurements. At 15 L min^{-1} injection rate, spatial correlation coefficients between Layer 4 (the uppermost layer) and the other layers decreased due to a change of the general shape of the upwelling flume (Figure 3f and Figure 9a.6 and b.6). Due

to the intense injection rate, the warm water signal travels straight upwards, and once it reaches the water surface, it spreads horizontally at the water surface.

4.2 | Relevance of diurnal cycle and cloud cover on signal detectability

Under overcast conditions, calculated slow energy changes (ΔE) over time and low net heat fluxes across the water surface (G) seem to be related to the spatial patterns in Figure 3d–f and the results obtained with the Moran's I coefficient, LISA maps, and the spatial correlation coefficients. Slow changes of energy (ΔE) over time and low net heat fluxes across the water surface (G) indicate that the mesocosm is able to sustain internal energy for longer time periods than under clear sky conditions. This means that the heat signal related to warm water injection is not lost. On the contrary, in datasets under clear and partly cloudy conditions, higher energy changes (ΔE) over time and higher net heat fluxes across the water surface (G) were calculated. In other words, the mesocosm loses internal energy faster over time, and consequently, the heat signal related to warm water injection is lost faster over time under clear sky conditions.

The amount of energy in a water body (for instance, a lake) is controlled by the inflows and outflows of water into and out of the water body and by heat fluxes across the water surface, among others (Henderson-Sellers, 1986). The net heat fluxes across the water surface (G) are composed of net shortwave radiation (R_{ns}), net longwave radiation (R_{nl}) and nonradiative fluxes (sensible heat [H] and latent heat [λE]; Henderson-Sellers, 1986; McAlister & McLeish, 1969). The main
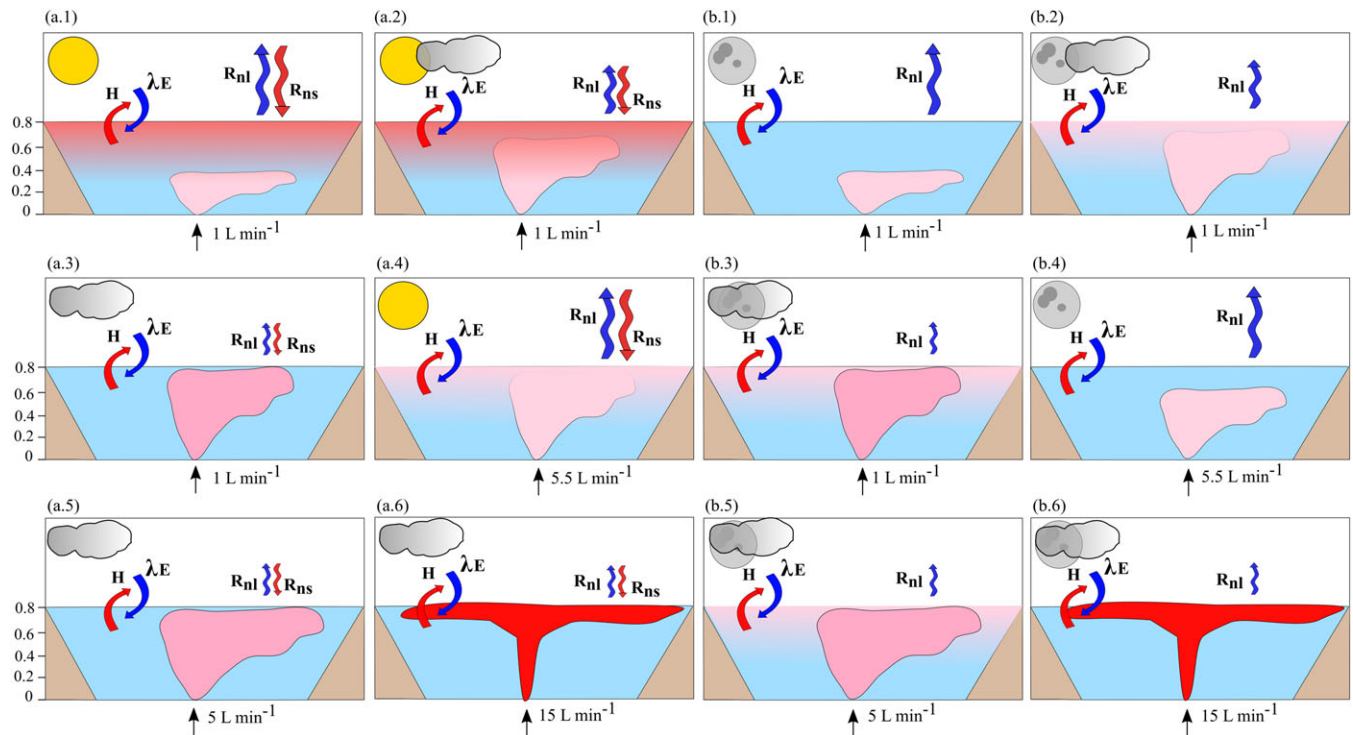

FIGURE 9 Conceptual model of spatial distribution of injected water in the water column under different weather conditions, for different injection rates during (a) day and (b) night. (a.1) and (b.1) 1 L min^{-1}, clear sky; (a.2) and (b.2) 1 L min^{-1}, partly cloudy sky; (a.3) and (b.3) 1 L min^{-1}, overcast sky; (a.4) and (b.4) clear sky, 5.5 L min^{-1}; (a.5) and (b.5) 5 L min^{-1}, overcast sky; (a.6) and (b.6) 15 L min^{-1}, overcast sky. The degree of the signal strength is indicated by the intensity of the red colour: Light red: weak signal, dark red: strong signal. The size of the arrows indicates the strength of the R_{nl} and R_{ns}. The blue colour indicates the losses of energy from the mesocosm. The red colour indicates the gains of energy in the mesocosm

component for calculated net heat fluxes across the water surface (G) is the net radiation (R_n), which is the sum of net shortwave radiation (R_{ns}) and net longwave radiation (R_{nl}). The net radiation balance is driven by the diurnal cycle of the incident shortwave radiation (Betts, 2015). This means that the solar warming during daytime and the longwave cooling during night-time drive the diurnal cycles of air temperature and water surface temperature (Betts, 2015; Vercauteren et al., 2011) and, thus, impact on the detectability of the injected warm water temperature signal in the mesososm.

Furthermore, cloud cover is also a relevant regulator of the diurnal cycle of the net radiation balance (R_n; Betts, 2003, 2015; Betts et al., 2013; Dai & Trenberth, 1999). Clouds decrease the incident shortwave radiation at the water surface and decrease the net surface cooling at the water surface because there is less R_{nl}.

Therefore, the detectability of the injected warm water temperature signal in the mesocosm is decisively controlled by the diurnal cycle of the net radiation balance (R_n) and the cloud cover.

In order to illustrate the relevance of the diurnal cycle (day vs. night) of the net radiation balance ($R_n = R_{ns} + R_{nl}$) and cloud cover on the observed spatial patterns of the heat signal related to warm water injection and based on the results presented in this paper, a conceptual model for the spatial patterns observed under different weather conditions (clear, partly cloudy, and overcast), injection rates, and diurnal cycles (day vs. night) is suggested in Figure 9. It illustrates the relevance of the net heat fluxes across the water surface (G) by the strength of net short wave (R_{ns}) and net long wave (R_{nl}) radiation (conceptualized by size of arrow: big: high values, small: low values) for different injection rates, different weather conditions (clear, partly cloudy, and overcast), and diurnal cycles (day vs. night). During day, the main gains or losses of heat at the mesocosm's water surface are due to the R_n ($=R_{ns} + R_{nl}$). During clear sky conditions during daytime, due to the higher solar warming (R_{ns}) at the water surface than during overcast weather conditions, the water surface is heated up. In consequence, the heat signal of the injected warm water at the water surface is mixed with the heated water surface due to solar warming. On the contrary, during overcast weather conditions during daytime, calculated R_n (see Figure 7) and solar warming due to R_{ns} are lower. In consequence, the heat signal of the injected warm water can be detected at the water surface (see Figure 9a).

During night, because there is no R_{ns}, the main gains or losses of heat at the mesocosm's water surface are due to R_{nl}. Both, during night and day, the degree of heat losses from the water surface depends on the presence of clouds at the sky (see Figure 9b). During clear sky conditions, the strength of R_{nl} is higher than under overcast weather conditions. In consequence, during clear sky conditions at night, the mesocosm loses higher amounts of energy across the water surface–atmosphere interface than during overcast conditions. The heat signal of the injected warm water at the water surface is lost faster during clear sky conditions than during overcast conditions at night (Figure 9b).

4.3 | Application of FO-DTS for detection of LGD upwelling

FO-DTS has been used to detect GW discharge at the sediment–water interface in lakes (Blume et al., 2013; Liu et al., 2015; Tristram et al.,

2015) and streams (Hare et al., 2015; Krause et al., 2012; Lowry et al., 2007). However, it had not yet been determined how the temperature signal propagates from the sediment–water interface through the water column up to the water surface–atmosphere interface and how the signal is affected by environmental parameters such as weather conditions (clear vs. overcast) and the diurnal cycle of net radiation. In Hare et al. (2015), FO-DTS measurements were compared with thermal infrared (TIR) measurements, which allowed the comparison of heat signals detected at the stream bed and at the water surface. Winter conditions were proven to be the best season to conduct these kinds of measurements. However, the characterization of weather and diurnal conditions that might have affected the upwelling patterns of the GW heat signal across the water column was not addressed until the present study. For instance, Liu et al. (2015) conducted an experiment on the lake bed that took into account environmental factors to determine the best time to detect GW discharge areas with FO-DTS. Liu et al. (2015) worked in a lake that was relatively shallow, which reduced the effect of vertical stratification on the lakebed temperatures during the FO-DTS measurements. Nevertheless, the FO-DTS experiment conducted did not include multilevel temperature measurements or a detailed characterization of the influence of weather conditions and the diurnal cycle of net radiation on the detection of GW discharge across the water column.

The knowledge gap on upwelling GW heat signals monitored with FO-DTS across the water column may have led to misinterpretations. This is because the temperature within the water column may be affected by several external parameters. Therefore, timing and conditions when measuring warm upwelling fluxes with FO-DTS are of great relevance for the interpretation of the results. For instance, it is crucial to be aware of the vertical positioning of the cable because variations of the vertical positioning of the cable on the sediment or within the water column may lead to misinterpretations of the patterns observed. Variable external conditions have to be taken into account for correct interpretation that might present a real difficulty for any quantitative assessment. Therefore, it is essential to determine those parameters that may influence the temperature such as solar radiation and to make sure that the temperature variations of the lake as detected by the FO-DTS are mainly caused by GW discharge (Liu et al., 2015) as presented in this paper.

4.4 | Possible system interferences and uncertainties of the study

4.4.1 | Effect of wind and possible consequences

Wind is an important factor affecting lake SW temperatures and lake internal mixing (Pöschke et al., 2015). Wind promotes movement and mixing of SW bodies. The SW can be dragged by the wind from one shore of a lake to the other shore inducing downwelling of water in the water body on one side of the lake and at the same time water movement from the bottom of the lake upwards to the lake surface (mixing). This process, relevant in lake settings, is probably irrelevant in the small experimental mesocosm used in the present study. From the slice3D plots in Figure 3, there is no indication for a wind-induced circulation or mixing. Wind speeds during the experiments were generally low (ranging from 0.0045 to 2.1789 m s^{-1}). Steep bank slopes

reaching a height of 1 m above the water surface prohibited wind impacts on the water surface. Furthermore, due to the small size of the mesocosm, the wind fetch is short and a potential wind impact on the water surface is irrelevant. However, when transferring the results of the mesocosm experiment to a real lake setting, possible wind impacts should be taken into account.

4.4.2 | Thickness of water column in the present study

In the present study, the thickness of the water column is 0.82 m. The obtained conclusions could be directly transferred to shallow lakes not deeper than 1 m, shore areas of lakes not deeper than 1 m, and probably to shallow lakes with slightly larger depth. Because there is no thermal stratification within the water column of the mesocosm, the obtained results of the present study can only be transferred to cases where there is no thermal stratification.

4.4.3 | Possible effects of electrical conductivity of GW

The upwelling of the water injected at the mesocosm's bottom is driven by density differences of the injected water and the water in the mesocosm. The density differences are caused by different temperatures and different ion compositions of the two waters. The water in the mesocosm is a mixture of lake water and water previously injected at the mesocosm's bottom. Due to differing injection rates during the different experiments, there is no constant relationship between the relatively large inflow from the lake (33 L min^{-1}) and the relatively small inflow from the injection at the mesocosm's bottom (0 to 15 L min^{-1}). For simplicity, we assume that the mesocosm water composition is basically identical to the lake water composition. On the basis of measurements of the ion composition of both water bodies, we ended up with total dissolved solid concentrations of 489 mg L^{-1} for the lake and 429 mg L^{-1} for the injected water, that is, there is a density difference of 60 mg L^{-1} between the two waters. Based on a mean mesocosm temperature of 4.7 °C, the density of the water in the mesocosm is 0.999946 kg L^{-1}, and based on a mean temperature of 15 °C of the injected water, the density is 0.999114 kg L^{-1}, that is, there is a density difference of 832 mg L^{-1} between the two waters. Basically, the density difference due to the different ion composition of the two different waters, strengthen the temperature induced density difference. The combined effect of ion composition and temperature on the density difference between the two waters is 880 mg L^{-1} (calculation according to Dietz, Lessmann, & Boehrer, 2012) or 921 mg L^{-1} (calculation according to Boehrer & Herzsprung, 2010).

Therefore, the injected warm water should immediately rise upwards through the surrounding denser lake water via buoyancy. During the short ascent, some mixing might have occurred and the contact with surrounding water resulted in some cooling of the injected warm water. Nevertheless, only in experiments during overcast conditions (Figure 3d–f), the injected warm water was still warmer than the rest of the water in the mesocosm when it reached the water surface and thus, floated on the top of the water body. From there, the warmer less dense water gradually spread as a plume on the water surface.

Low wind speeds, shallow water conditions, and density differences between simulated GW and SW might favour the upwelling of simulated GW discharge on the SW. However, in the present study, the main parameters controlling the detection of simulated GW on the water surface seem to be the net radiation balance (R_n) and the cloud cover during day and night-time measurements. Because the experiments have been carried out under specific conditions, the previous statements are only true in lake areas where the same conditions apply as in the mesocosm experiment during winter conditions.

This study is a first attempt to simulate thermal patterns of discrete LGD in shallow lakes or close to lake shores. The mesocosm experiment and simulation of GW discharge is the first step in order to identify the main controlling parameters that favour detection of hotspots of LGD on the lake surface (mesocosm surface in this case). We have decreased the amount of variables that impact LGD by simulating discrete GW discharge in a mesocosm. The mesocosm where the simulation has been performed intends to represent a small shallow area of a lake where GW exfiltration by LGD occurs. Thus, not all the influencing factors such as wind, waves, and vegetation that could be present under natural conditions have been considered. However, GW discharge that is warmer than SW has been little studied relative to discharge of cold GW to warmer SW. Thus, by conducting studies during colder times of the year, scientist can make use of the conclusions presented here.

5 | CONCLUSION

The present study demonstrates that during winter conditions, the positive buoyancy of relatively warm water imported by simulated LGD into shallow water bodies (mesocosm used as model system) allows detection of LGD at the lake's water surface–atmosphere interface by FO-DTS. FO-DTS technology offers fine scale measurements with high temporal resolution and allows the observation of induced lake-internal upwelling caused by simulated LGD in a three-dimensional perspective. In this manner, different lake internal upwelling patterns have been described from the sediment–water interface through the water column to the water surface–atmosphere interface caused by the injection of warm water at different rates, different weather conditions, and during the diurnal cycle. Simulated GW signals at the water surface were identified at all applied injection rates, from lowest 1 L min^{-1} to highest 15 L min^{-1}. However, detection of simulated LGD at the water surface–atmosphere interface was mainly determined by the diurnal cycle of the net radiation balance (R_n) and the cloud cover.

Based on the results presented in this paper, overcast weather conditions and night-time measurements are recommended for tracing discrete warm water upwelling fluxes across the water column and at the water surface.

ORCID

Amaya Irene Marruedo Arricibita http://orcid.org/0000-0001-7992-4609

Stefan Krause http://orcid.org/0000-0003-2521-2248

Jesus Gomez-Velez http://orcid.org/0000-0001-8045-5926

David M. Hannah http://orcid.org/0000-0003-1714-1240

Jörg Lewandowski http://orcid.org/0000-0001-5278-129X

REFERENCES

Anselin, L. (1995). Local indicators of spatial association—LISA. *Geographical Analysis*, *27*(2), 93–115. https://doi.org/10.1111/j.1538-4632.1995.tb00338.x.

Anselin, L. (1996). The Moran scatterplot as an ESDA tool to assess local instability in spatial association. In *Spatial analytical perspectives on GIS* (pp. 111–125).

Apperl, B., Pressl, A., & Schulz, K. (2017). Feasibility of locating leakages in sewage pressure pipes using the distributed temperature sensing technology. *Water, Air, and Soil Pollution*, *228*(2). https://doi.org/10.1007/s11270-017-3250-7.

Baker, B. H., Martinovic-Weigelt, D., Ferrey, M., Barber, L. B., Writer, J. H., Rosenberry, D. O., ... Schoenfuss, H. L. (2014). Identifying non-point sources of endocrine active compounds and their biological impacts in freshwater lakes. *Archives of Environmental Contamination and Toxicology*, *67*(3), 374–388. https://doi.org/10.1007/s00244-014-0052-4.

Betts, A. K. (2003). The diurnal cycle over land. In M. Mencuccini, J. Grace, J. Moncrieff, & K. McNaughton (Eds.), *Forests at the land-atmosphere interface* (pp. 73–93). Wallingford, Oxon OX10 8DE, UK: CABI Publishing.

Betts, A. K. (2015). Diurnal Cycle. In J. Pyle, & Z. Fuqing (Eds.), *Encyclopedia of atmospheric sciences* (pp. 319–323). College Station, TX, USA: Texas A&M University https://doi.org/10.1016/B978-0-12-382225-3.00135-3.

Betts, A. K., Desjardins, R., & Worth, D. (2013). Cloud radiative forcing of the diurnal cycle climate of the Canadian Prairies. *Journal of Geophysical Research*, *118*(June), 8935–8953. https://doi.org/10.1002/jgrd.50593.

Bivand, R. S., Pebesma, E., & Gómez-Rubio, V. (2013). *Applied spatial data analysis with R*. New York: Springer-Verlag. https://doi.org/10.1007/978-1-4614-7618-4.

Blume, T., Krause, S., Meinikmann, K., & Lewandowski, J. (2013). Upscaling lacustrine groundwater discharge rates by fiber-optic distributed temperature sensing. *Water Resources Research*, *49*(October 2012), 7929–7944. https://doi.org/10.1002/2012WR013215.

Boehrer, B., & Herzsprung, P. (2010). Calculating density of water in geochemical lake stratification models. *Limnology and oceanography, methods*, *1*, 567–574. https://doi.org/10.4319/lom.2010.8.567.

Brabrand, Å., Koestler, A. G., & Borgstrøm, R. (2002). Lake spawning of brown trout related to groundwater influx. *Journal of Fish Biology*, *60*(3), 751–763. https://doi.org/10.1006/jfbi.2002.1901.

Brunke, M., & Gonser, T. (1997). The ecological significance of exchange processes between rivers and groundwater. *Freshwater Biology*, *37*, 1–33. https://doi.org/10.1046/j.1365-2427.1997.00143.x.

Cardenas, M. B., Lagmay, A. M. F., Andrews, B. J., Rodolfo, R. S., Cabria, H. B., Zamora, P. B., & Lapus, M. R. (2012). Terrestrial smokers: Thermal springs due to hydrothermal convection of groundwater connected to surface water. *Geophysical Research Letters*, *39*(2), 1–6. https://doi.org/10.1029/2011GL050475.

Curry, R. A., & Noakes, D. L. G. (1995). Groundwater and the selection of spawning sites by brook trout (Salvelinus fontinalis). *Canadian Journal of Fisheries and Aquatic Sciences*, *52*(8). https://doi.org/10.1139/f95-765.

Dai, A., & Trenberth, K. E. (1999). Effects of clouds, soil moisture, precipitation, and water vapor on diurnal temperature range. *Journal of Climate*, *12*, 2451–2473.

Dietz, S., Lessmann, D., & Boehrer, B. (2012). Contribution of solutes to density stratification in a meromictic Lake (Waldsee/Germany). *Mine Water and the Environment*, *31*(2), 129–137. https://doi.org/10.1007/s10230-012-0179-3.

Environmental Systems Research Institute (2014). ArcGIS desktop help 10.3: How band collection statistics works. Available at: http://desktop.arcgis.com/en/arcmap/10.3/tools/spatial-analyst-toolbox/how-band-collection-statistics-works.htm#GUID-FE2BAE08-24DB-4A50-8F88-86D856F89190 [Accessed 15 March 2016]

Hare, D. K., Briggs, M. A., Rosenberry, D. O., Boutt, D. F., & Lane, J. W. (2015). A comparison of thermal infrared to fiber-optic distributed temperature sensing for evaluation of groundwater discharge to surface water. *Journal of Hydrology*, *530*, 153–166. https://doi.org/10.1016/j.jhydrol.2015.09.059.

Haselwimmer, C., Prakash, A., & Holdmann, G. (2013). Quantifying the heat flux and outflow rate of hot springs using airborne thermal imagery: Case study from Pilgrim Hot Springs, Alaska. *Remote Sensing of Environment*, *136*, 37–46. https://doi.org/10.1016/j.rse.2013.04.008.

Hausner, M. B., Suárez, F., Glander, K. E., van de Giesen, N., Selker, J. S., & Tyler, S. W. (2011). Calibrating single-ended fiber-optic Raman spectra distributed temperature sensing data. *Sensors*, *11*(11), 10859–10879. https://doi.org/10.3390/s111110859.

Hayashi, M., & Rosenberry, D. (2002). Effects of ground water exchange on the hydrology and ecology of surface water. *Ground Water*, *40*(3), 309–316.

Henderson-Sellers, B. (1986). Calculating the surface energy balance for lake and reservoir modeling: A review. *Reviews of Geophysics*, *24*(3), 625. https://doi.org/10.1029/RG024i003p00625.

Hung, Y.-T., Eldridge, J., Taricska, J. R., & Li, K. H. (2005). In L. K. Wang, N. C. Pereira, & Y.-T. Hung (Eds.), *Advanced air and noise pollution control* (pp. 359–384). Totowa, NJ: Humana Press DOI: https://doi.org/10.1007/978-1-59259-779-6_10.

Kidmose, J., Engesgaard, P., Nilsson, B., Laier, T., & Looms, M. C. (2011). Spatial distribution of seepage at a flow-through Lake: Lake Hampen, Western Denmark. *Vadose Zone Journal*, *10*(1), 110. https://doi.org/10.2136/vzj2010.0017.

Krause, S., Blume, T., & Cassidy, N. J. (2012). Investigating patterns and controls of groundwater up-welling in a lowland river by combining fibre-optic distributed temperature sensing with observations of vertical hydraulic gradients. *Hydrology and Earth System Sciences*, *16*(6), 1775–1792. https://doi.org/10.5194/hess-16-1775-2012.

Lewandowski, J., Meinikmann, K., Ruhtz, T., Pöschke, F., & Kirillin, G. (2013). Localization of lacustrine groundwater discharge (LGD) by airborne measurement of thermal infrared radiation. *Remote Sensing of Environment*, *138*, 119–125. https://doi.org/10.1016/j.rse.2013.07.005.

Liu, C., Liu, J., Wang, X., & Zheng, C. (2015). Analysis of groundwater-lake interaction by distributed temperature sensing in Badain Jaran Desert, Northwest China. *Hydrological Processes*. https://doi.org/10.1002/hyp.10705.

Lowry, C. S., Walker, J. F., Hunt, R. J., & Anderson, M. P. (2007). Identifying spatial variability of groundwater discharge in a wetland stream using a distributed temperature sensor. *Water Resources Research*, *43*(10), n/a-n/a DOI: https://doi.org/10.1029/2007WR006145.

McAlister, E. D., & McLeish, W. (1969). Heat transfer in the top millimeter of the ocean. *Journal of Geophysical Research*, *74*(13), 3408–3414. https://doi.org/10.1029/JC074i013p03408.

Nakayama, T., & Watanabe, M. (2008). Missing role of groundwater in water and nutrient cycles in the shallow eutrophic Lake Kasumigaura, Japan. *Hydrological Processes*, *22*, 1150–1172. https://doi.org/10.1002/hyp.6684.

Norrström, A. C., & Jacks, G. (1996). Water pathways and chemistry at the groundwater/surface water interface to Lake Skjervatjern, Norway. *Water Resources Research*, *32*(7), 2221–2229. https://doi.org/10.1029/96WR00802.

Piña-Ochoa, E., & Lvarez-Cobelas, M. (2009). Seasonal nitrogen dynamics in a seepage lake receiving high nitrogen loads. *Marine and Freshwater Research*, *60*(5), 435–445. https://doi.org/10.1071/MF08098.

Pöschke, F., Lewandowski, J., Engelhardt, C., Preuß, K., Oczipka, M., Ruhtz, T., & Kirillin, G. (2015). Upwelling of deep water during thermal stratification onset—A major mechanism of vertical transport in small temperate lakes in spring? *Water Resources Research*, https://doi.org/10.1002/2015WR017579.

Ridgway, M. S., & Blanchfield, P. J. (1998). Brook trout spawning areas in lakes. *Ecology of Freshwater Fish*, 7, 140–145. https://doi.org/10.1111/j.1600-0633.1998.tb00180.x.

Rosenberry, D. O., Lewandowski, J., Meinikmann, K., & Nützmann, G. (2015). Groundwater—The disregarded component in lake water and nutrient budgets. Part 1: Effects of groundwater on hydrology. *Hydrological Processes*, 29(13), 2895–2921. https://doi.org/10.1002/hyp.10403.

Sebok, E., Duque, C., Kazmierczak, J., Engesgaard, P., Nilsson, B., Karan, S., & Frandsen, M. (2013). High-resolution distributed temperature sensing to detect seasonal groundwater discharge into Lake Væng, Denmark. *Water Resources Research*, 49(9), 5355–5368. https://doi.org/10.1002/wrcr.20436.

Selker, J. S., Thévenaz, L., Huwald, H., Mallet, A., Luxemburg, W., van de Giesen, N., … Parlange, M. B. (2006). Distributed fiber-optic temperature sensing for hydrologic systems. *Water Resources Research*, 42(12), n/a-n/a https://doi.org/10.1029/2006WR005326.

Selker, J. S., Tyler, S., & Van de Giesen, N. (2014). Comment on 'capabilities and limitations of tracing spatial temperature patterns by fiber-optic distributed temperature sensing' by Liliana Rose et al. *Water Resources Research*, 50, 5372–5374. https://doi.org/10.1002/2013WR014979.

Selker, J. S., van de Giesen, N., Westhoff, M., Luxemburg, W., & Parlange, M. B. (2006). Fiber optics opens window on stream dynamics. *Geophysical Research Letters*, 33(24), L24401 https://doi.org/10.1029/2006GL027979.

Shuster, W. W. (1986). In L. K. Wang, & N. C. Pereira (Eds.), *Water resources and natural control processes* (pp. 107–138). Totowa, NJ: Humana Press. https://doi.org/10.1007/978-1-4612-4822-4_3.

Tristram, D. A., Krause, S., Levy, A., Robinson, Z. P., Waller, R. I., & Weatherill, J. J. (2015). Identifying spatial and temporal dynamics of proglacial groundwater—Surface-water exchange using combined temperature-tracing methods. *Freshwater Science*, 34(October 2013), 99–110. https://doi.org/10.1086/679757.

van de Giesen, N., Steele-Dunne, S. C., Jansen, J., Hoes, O., Hausner, M. B., Tyler, S., & Selker, J. (2012). Double-ended calibration of fiber-optic Raman spectra distributed temperature sensing data. *Sensors*, 12(5), 5471–5485. https://doi.org/10.3390/s120505471.

Vercauteren, N., Huwald, H., Bou-Zeid, E., Selker, J. S., Lemmin, U., Parlange, M. B., & Lunati, I. (2011). Evolution of superficial lake water temperature profile under diurnal radiative forcing. *Water Resources Research*, 47, 1–10. https://doi.org/10.1029/2011WR010529.

Warren, D. R., Sebestyen, S. D., Josephson, D. C., Lepak, J. M., & Kraft, C. E. (2005). Acidic groundwater discharge and in situ egg survival in redds of lake-spawning brook trout. *Transactions of the American Fisheries Society*, 134(5), 1193–1201. https://doi.org/10.1577/T04-180.1.

SUPPORTING INFORMATION

Additional Supporting Information may be found online in the supporting information tab for this article.